Communication

Electromagnetic Transmit Array With Optical Control for Beamforming

Wei Zhang[®], Javad Meiguni[®], Yin Sun[®], Muqi Ouyang[®], Xin Yan[®], Xu Wang[®], Reza Yazdani[®], Daryl Beetner[®], Donghyun Kim[®], and David Pommerenke[®]

Abstract— This proof-of-concept communication demonstrates the feasibility of using a slide projector to steer the beam of a transmit array by adding solar cells and varactor diodes to each unit cell. By irradiating each solar cell with the light of different intensities from a slide projector, the measured phase of the wave transmitted by the 4 \times 4 transmit array shifts within 92° at 4.26 GHz, while the variation in magnitude is measured within 4 dB. Different light configurations are identified via a searching algorithm to achieve peak/null beamforming in a particular direction. The beam of the prototypical 4 \times 4 transmit array can be shifted by $\pm 24^\circ$ in terms of the peaks and -30° to 36° in terms of nulls. The concept of adding light modulation to the transmit array with a slide projector can provide update rates of tens of milliseconds with control of brightness and color distributed over a large area of the array.

Index Terms—Beamforming, light modulation, reconfigurable slide projector, transmit array, varactor diodes.

I. INTRODUCTION

Transmit array antennas are used to produce a focused beam but without the need for the feed structures of traditional antenna arrays. Various structures of transmit array antennas have been discussed in [1], [2], and [3], with each implementation improving characteristics such as efficiency, bandwidth, or cross polarization.

In addition, reconfigurable transmit arrays have been investigated for their flexibility in controlling the beam direction. Controllable beamforming can be achieved with a tunable phase shifter in each element of a transmit array. In [4], it was discussed that there are generally two approaches for designing a transmit array: 1) the layer-scattered approach and 2) the guided-wave approach. In the layer-scattered approach, multilayer frequency-selective surfaces (FSSs) with different design parameters were used to achieve the phase shift [4]. In the guided-wave approach, individual antenna and guided-wave phase shifter were used to achieve power reception, phase shift, and power transfer [4], [5]. Other methods, such as using controllable antenna directors, were also used to achieve reconfigurable transmit arrays. In [6] and [7], transmit arrays were designed with plasma tubes with a controllable arrangement as antenna directors.

Manuscript received 21 July 2022; revised 23 March 2023; accepted 23 March 2023. Date of publication 18 April 2023; date of current version 2 June 2023. This work was supported in part by the National Science Foundation (NSF) under Grant IIP-1916535. (Corresponding author: Wei Zhang.)

Wei Zhang, Javad Meiguni, Yin Sun, Muqi Ouyang, Xin Yan, Xu Wang, Reza Yazdani, Daryl Beetner, and Donghyun Kim are with the Electromagnetic Compatibility (EMC) Laboratory, Missouri University of Science and Technology, Rolla, MO 65409 USA (e-mail: wznkm@mst.edu; javad.meiguni@mst.edu; ysc26@mst.edu; ouyangm@mst.edu; yx9n9@mst.edu; xw7dh@mst.edu; ry2kw@mst.edu; daryl@mst.edu; dkim@mst.edu).

David Pommerenke is with the Graz EMC Laboratory, Graz University of Technology, 8010 Graz, Austria, and also with the Electromagnetic Compatibility (EMC) Laboratory, Silicon Austria Labs, 8010 Graz, Austria (e-mail: david.pommerenke@ieee.org).

Color versions of one or more figures in this communication are available at https://doi.org/10.1109/TAP.2023.3266871.

Digital Object Identifier 10.1109/TAP.2023.3266871

For a tunable phase shifter, methods, such as p-i-n-diodes, varactor diodes, microelectromechanical systems (MEMS) switches, and liquid crystals (LCs), have been used as the active element that converts the control signal into a variable electromagnetic (EM) response. In [8], [9], [10], and [11] transmit array structures were presented using a 1-bit phase shift technique implemented by a p-i-n-diode. In [12], a transmit array based on monolithic integrated MEMS switches was designed with a $\pm 40^{\circ}$ beam steering capacity. In [13], a switched focal array was designed to achieve 1-, 2-, and 2.8-bit phase control by using flip-chip mounted single-pole threeway throw (SP3T) switches. In [4], [14], and [15], transmit arrays with guided-wave phase shifter were proposed by integrating varactor diodes into the phase shifter structure. Moreover, LC molecules of tunable permittivity with varying bias voltages have been applied to reflect arrays [16], [17] and a transmit array [18]. However, the reconfigurable transmit arrays discussed above use electrical control of the phase shifter, which leads to unavoidable complexity caused by the metallic bias control network. The optical modulation technique is a promising approach for the design of the reconfigurable transmit array to provide analog control of the phase of each element. This avoids the numerous wires for electrical control required in a large array.

Light modulation was used in the design of a tunable metamaterial structure with varactor diodes or photodiodes [19], [20], [21], and [22] tunable plasma reflectors for beamforming purposes [23]. In [24], a silicon-based photoconductive metamaterial was designed as a THz absorber. The designed reflect array showed tunable frequency ranges of absorption under different spatial light distributions without variation on light intensities [24]. In [25], [26], and [27], organic semiconductor poly (3-hexylthiophene) (P3HT) was used within an optically controlled phase shifterin an antenna array. Because it is a small bandgap (around 1.9 eV), it absorbs light between 450 and 600 nm. In [28], a laser was used to generate plasma for designing a plasma-based reflector. From the work discussed, most of the light sources for optical control were LEDs [19], [20], [21], [22], and [26], spatial light modulator/digital micromirror devices [24], laser [28], and tungsten filament microscope light source [25].

A slide projector can provide different colors and brightness control, update rates of tens of milliseconds, and cover a large area that can be used as a light source. A solar cell can provide a dc bias voltage to control the capacitance of a varactor diode. To the authors' knowledge, there are still few transmit array designs that take advantage of tuning light intensity and spatial distribution from a slide projector in combination with unit cells that use varactor diodes and solar cells. The novelty of this communication lies in demonstrating the feasibility of this concept in simulation and validating it through measurements. The advantage over electrically controlled arrays increases with the number of elements in the array. Besides, the light-modulated method with solar cells uses wireless power, which can significantly avoid redundant electrical connections for phase shift controlling and reduce the risk of issues related to electrical control and connection.

0018-926X © 2023 IEEE. Personal use is permitted, but republication/redistribution requires IEEE permission. See https://www.ieee.org/publications/rights/index.html for more information.

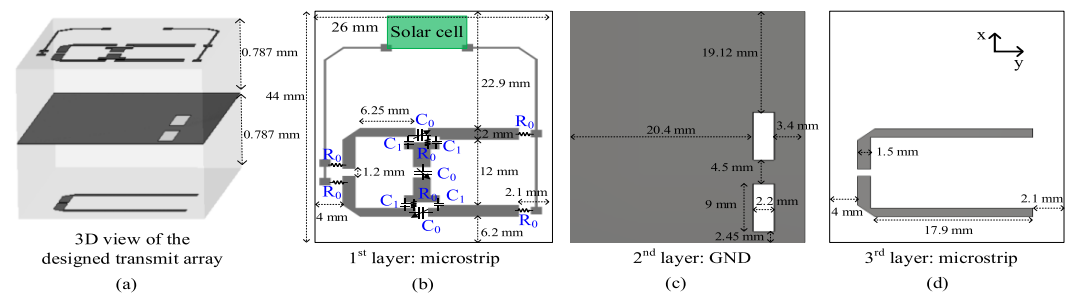


Fig. 1. Unit cell structure of each layer. (a) Three-dimensional view of the designed transmit array. (b) First layer: microstrip. (c) Second layer: GND. (d) Third layer: microstrip.

II. UNIT CELL AND ARRAY DESIGN

A. Description of Unit Cell

The diagram of the unit cell structure is shown in Fig. 1(a)–(d). It is designed on a three-layer printed circuit board (PCB) inspired by those shown in [4] and [14]. In this work, since the author wanted to provide a proof of concept of light modulation on the beamforming of a transmit array, the patch antennas on the top and bottom layers for receiving and transmitting the EM energy were removed for simplicity. Instead of a microcontroller and electrical connections, solar cells are used for fast optical control. The fabricated three-layer PCB consists of two two-layer PCBs, each with the same GND structure on one side. The two GND layers of the two PCBs are glued together to form a three-layer PCB. Rogers RT duroid 5870 material with a thickness of 0.787 mm is used for the PCB substrate. The detailed dimensions of the structure are shown in Fig. 1(b)–(d).

The first layer contains microstrip traces with a balanced bridged-T phase shifter [4], [14] in the middle. The gap in the x-direction between the microstrip lines at the left of Fig. 1(b) can pick up the E-field in the same direction and transfer the coupled energy to the balanced bridged-T phase shifter. The phase shifter contributes to beamforming. Resonances are generated by the equivalent inductance of the microstrip traces and the variable capacitances (C_0) of the varactor diodes. The varactor diode used in this work is Skyworks SMV1232-79LF, which can create equivalent capacitance in the range of 0.72-4.1 pF under the reverse bias voltage from 15 to 0 V. Therefore, the resonant frequency or phase (when a fixed frequency is observed) could be shifted by the variable capacitance. A solar cell (IXYS CPC1832N) was used to provide the reverse bias voltage for the varactor diode, which has the maximum open-circuit output voltage of up to 10 V. The miniature size $(6 \times 10 \times 1.7 \text{ mm})$ of the solar cell allows for easy installation on the transmit array in a compact space. Lumped components, such as R_0 (10 k Ω , 0603 package) and C₁ (180 pF, 0402 package), are for dc bias connections on the varactor diode. The equivalent circuit of the phase shifter and the corresponding phase shift capability has been discussed in [13]. The second layer contains a GND plane with two slots, which is the main structure for radiation. The current with shifted phase around the GND slots contributes to the radiation through the transmit array. The third layer contains two microstrip traces in an electric dipole shape similar to the first layer, but without the phase shifter. From aperture coupling, the phase-shifted signal in the first layer couples to microstrip trace in the third layer via the slots in the GND plane.

The radiation mechanism of this antenna is given as follows. The two slots on the second layer (GND layer) can act as slot antennas for EM reception and transmission. At the same time, due to the proximity effect, currents at the right end of the microstrip traces in the first layer in Fig. 1(b) can also affect the current around the slots in the second layer [29]. The microstrip structures in the first and third

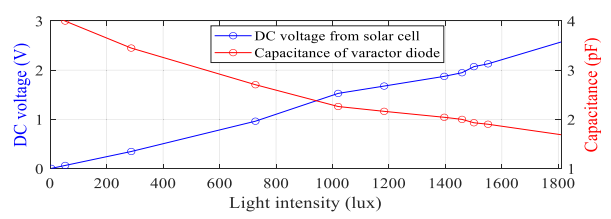


Fig. 2. DC voltage from the solar cell versus light intensity and capacitance of varactor diode versus light intensity.

layers improve the bandwidth and efficiency of the slot antennas on the GND layer. The EM energy from the incident wave (feed antenna) induces the electric and magnetic dipole moments for each current element in the first layer, including the microstrip lines and the gap in the *x*-direction between the microstrip lines. The microstrip lines are by design less radiative compared to the gaps in the first layer and the slots in the GND layer in the operating frequency. As a result, the induced EM waves received by the gap in the first layer propagate along both transmission lines and get a certain phase shift depending on the light profile and phase response of the varactor diodes. The EM fields coupled into the slots in the second layer (GND layer) with shifted phase determine the radiation of this transmit array antenna. The microstrip lines in the third layer carry the proximity-coupled EM wave to the 1.2-mm gap located on the left side, which improves the bandwidth and efficiency of the radiation from this transmit array.

Fig. 2 shows the measured dc bias voltage as a function of light intensity for the solar cell and the extracted capacitance of the varactor diode as a function of the light intensity, which is calculated from the relationship between the capacitance and bias voltage of the varactor diode in the datasheet. The test was performed by shining a grayscale image from a slide projector controlled by a laptop to the solar cell and measuring the dc voltages at the solar cell under different light intensities. The light intensity values were measured from 0 to 1800 lux through a digital light meter. The voltage varied from 0 to 2.7 V, providing a well-tuned range of capacitance between 4.1 and 1.5 pF for the varactor diode. The solar cell exhibited an approximately linear response of the dc voltage as a function of light intensity.

The structure of the unit cell was designed in CST Microwave Studio (MWS). The varactor diode was modeled as a capacitor of defined values and its resistance from the datasheet. By applying Floquet boundary conditions, the unit cell was automatically expanded to an infinite array and the plane wave excitation was assigned to interact with the infinite transmit array. By applying the incident plane wave with the *E*-field in the *y*-direction, the slots in the GND plane can be excited in the TM_{11} mode [30]. S_{21} is defined as the ratio between the magnitude of the transmitted plane wave through the structure and the magnitude of the incident plane wave to the structure. Fig. 3(a) and (b) shows the simulated S_{21} when the same capacitance (C_0 in Fig. 1) of the varactor diode was applied to

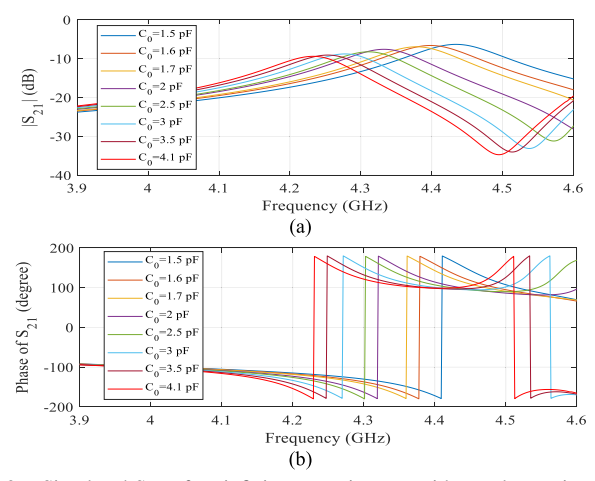


Fig. 3. Simulated S_{21} of an infinite transmit array with equal capacitance at each unit cell under the Floquet boundary condition. (a) Magnitude. (b) Phase.

Fig. 4. Setup of the radiation pattern simulation and the capacitance configuration applied to the 4×4 transmit array for phase tuning.

each unit cell for an infinite transmit array. It was observed that at 4.26 GHz, the simulated maximal phase change of S_{21} was 96° when C_0 varied between 1.5 and 4.1 pF. Meanwhile, the magnitude of S_{21} changed within 5 dB. As a result, the transmit array demonstrated a phase-shifted EM wave transmission capability with no significant change in magnitude.

B. Array Simulation

Fig. 4 shows the simulation model of a 4×4 transmit array mounted on a perfect electric conductor (PEC) shielding box with the C_0 capacitance for phase tuning in each unit cell. The simulation used a DEEPACE wideband omnidirectional dipole antenna (1.8–9 GHz) [31] mounted on the back wall of the shielding box as the excitation. The radiation patterns were observed for different capacitance (C_0 in Fig. 1) configurations. Four different cases were chosen as follows.

- 1) Case 0 (Reference Case): Shielding box without the transmit array. The front surface has a hole the same size as the transmit array.
- 2) Case 1: All unit cells with the same capacitance of 4.1 pF.
- 3) Case 2: Progressive capacitances of 4.1, 3, 2, and 1.5 pF from the left to the right column of the transmit array.
- 4) Case 3: Inverse progressive capacitances of Case 2.

Fig. 5 compares the H-plane radiation pattern transmitted through the array at 4.26 GHz. As the variation of capacitances is along the z-direction, the beam will be steered in the H-plane. The beam steering of $\pm 15^{\circ}$ for Cases 1 and 3 is observed in the simulated H-plane radiation pattern, proving that the design of the unit cell of the transmit array is reasonable.

III. MEASUREMENTS

A. Measurement Results

The fabricated PCB of a 4×4 transmit array is shown in Fig. 6(a). The PCB was mounted on the front wall of a shielding box, as shown

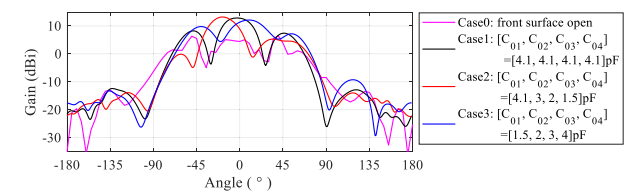


Fig. 5. Simulated H-plane radiation pattern (gain in dB) of a 4×4 array with different capacitance configurations.

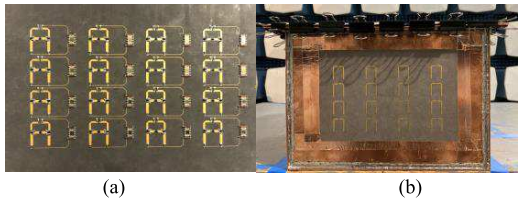


Fig. 6. Fabricated transmit array and shielding box. (a) First layer of the transmit array. (b) Transmit array mounted on the front wall of a shielding box.

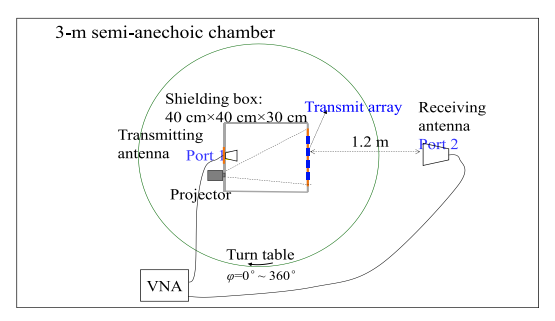
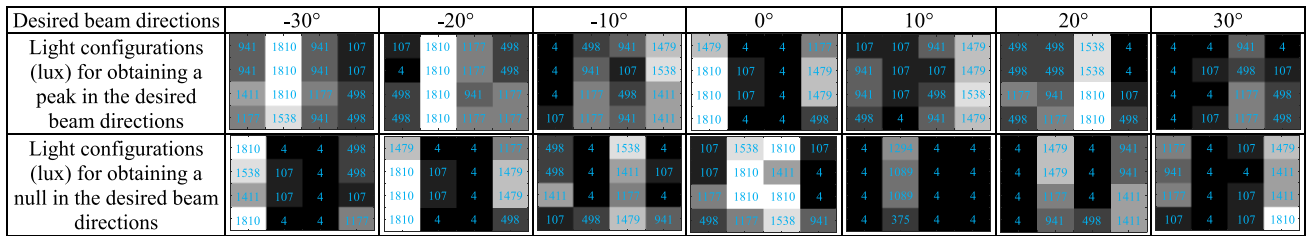


Fig. 7. Setup of the radiation pattern measurement in terms of $|S_{21}|$.

in Fig. 6(b). A DEEPACE wideband omnidirectional dipole antenna was mounted on the back wall as a source to create the EM wave that interacts with the designed transmit array. The shielding box was used to enforce the EM wave from the source antenna interacting with the transmit array without leaking outside the shielding box so that the receiving antenna measures only the radiation pattern of the transmitted EM wave through the transmit array. In addition, a projector placed outside the shielding box was used to shine light through a 2×2 cm shielding glass mounted on the back wall of the shielding box. Absorbers (Larid Eccorsorb QR-13AF with a thickness of 6.4 mm and 11.5-dB attenuation coefficient [32]) were mounted inside the shielding box to avoid cavity resonances.

The diagram for the measurement setup is shown in Fig. 7. The shielding box containing the transmit array was placed on a turntable with a height of 0.8 m. Considering the large size of the system, there are challenges to mount the system inside an anechoic chamber for 3-D radiation pattern measurements. Therefore, 2-D radiation patterns of the system were measured inside a 3-m semianechoic chamber to show the proof of concept of the design. A horn antenna (ETS-Lindgren's Model 3117) at 1.2 m from the transmit array was used to measure the EM wave transmitted through the transmit array. Although the distance between the DEEPACE wideband omnidirectional dipole antenna and the receiving antenna did not reach the rigorous far-field conditions, the feasibility of optically based beamforming was investigated for the proposed transmit array structure. The S₂₁ between the DEEPACE wideband omnidirectional dipole antenna and the horn antenna was measured under different illumination configurations. Fig. 8 shows the magnitude and phase of the measured S₂₁ when illuminating the same light intensity to all unit cells. Besides, |S₂₁| of a reference case was measured when the front face of the shielding box is open, i.e., the transmit array is removed/not mounted from the front face of the shielding box. The

TABLE I OPTIMIZED LIGHT CONFIGURATIONS FOR PEAKS/NULLS OF THE RADIATION PATTERN TOWARD THE DESIRED BEAM DIRECTIONS



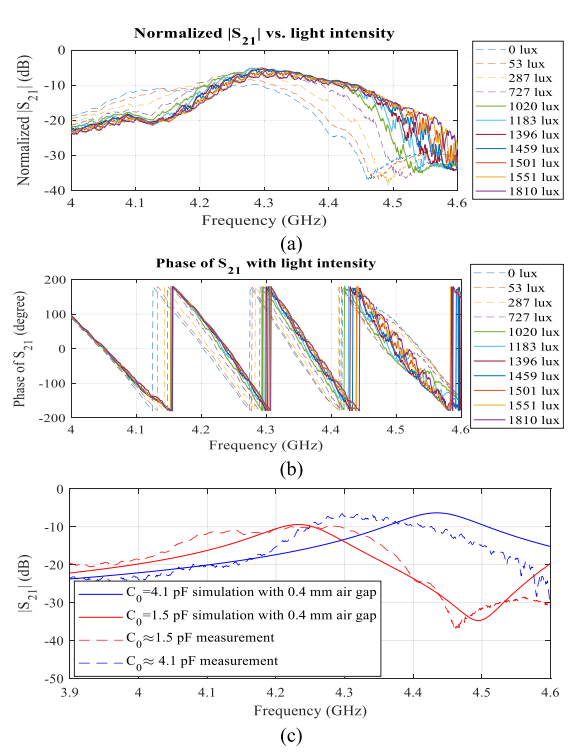


Fig. 8. Measured S_{21} response of a 4 \times 4 transmit array with different light intensities. (a) Magnitude (normalized to the reference case that no transmit array mounted in the front face of the shielding box). (b) Phase. (c) Comparison of $|S_{21}|$ between measurement and simulation.

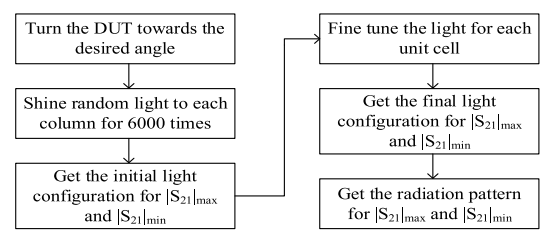


Fig. 9. Searching algorithm to find a light configuration to redirect the peak and null of radiation pattern to a certain direction.

 $|S_{21}|$ curves measured under different light intensities illuminating the transmit array were normalized to the reference, as shown in Fig. 8(a). It is observed that at the resonance frequency of 4.3 GHz, the total loss caused by the transmit array is between 5.5 and 10.5 dB, which can be explained by the reflection loss between the transmit array and the air, and the resistive loss from the resistances in the transmit array. However, as a proof-of-concept study, such loss of the transmit array may not be very critical if the light-controlled phase shift and beamforming behavior can be achieved. Fig. 8(b) shows when varying the light intensities from 0 to 1810 lux, the phase of S_{21} could be shifted by at most 92° at 4.26 GHz, while the magnitude of S_{21} changes within 4 dB. Fig. 8(c) compares $|S_{21}|$ between simulation and measurement. The simulation model considered a 0.4-mm air

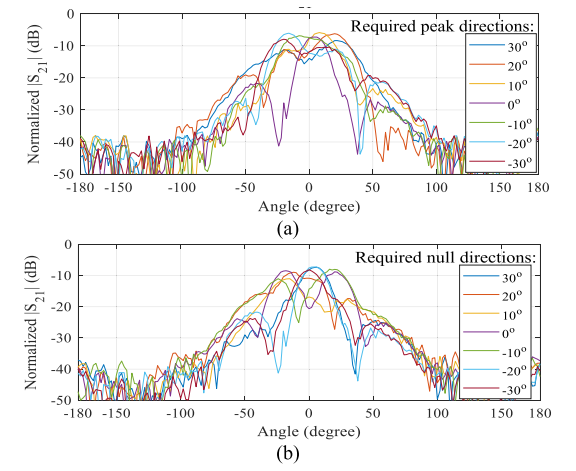


Fig. 10. Optimized radiation patterns (normalized $|S_{21}|$ in dB) in H-plane at 4.26 GHz for the desired peak and null direction of 30° , 20° , 10° , 0° , -10° , -20° , and -30° . (a) Peak directions. (b) Null directions.

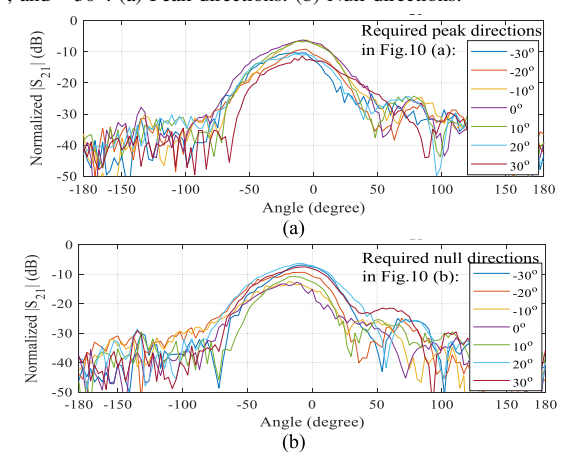
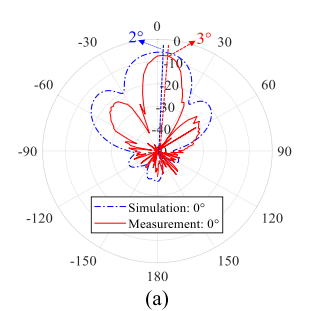
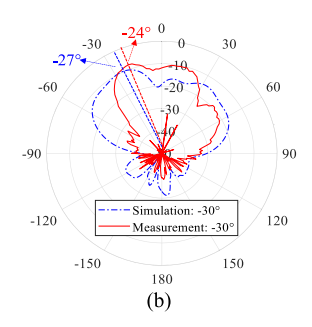


Fig. 11. Corresponded E-plane radiation patterns at 4.26 GHz under the same light configurations for required peak and null directions in H-plane in Fig. 10. (a) E-plane radiation patterns corresponding to Fig. 10(a). (b) E-plane radiation patterns corresponding to Fig. 10(b).

gap between the two PCBs of the transmit array during fabrication. Similarities between the measured and simulated results are observed in terms of resonant frequency and maximum phase shift.

Beamforming can be achieved by applying different light intensities to each unit cell. A searching algorithm was used to find the local optimal light configuration to redirect a peak or null of radiation to the desired direction. Fig. 9 shows the flowchart of the searching algorithm. First, a brute-force approach was used. The array was mechanically rotated to measure the 2-D radiation pattern. Then, $|S_{21}|$ at 4.26 GHz was searched by randomly adjusting the light configuration at each column in the transmit array, where all unit cells within a column were illuminated with the same light intensity. Once the optimal configuration was identified from the random search, the light intensities for unit cells in each column were





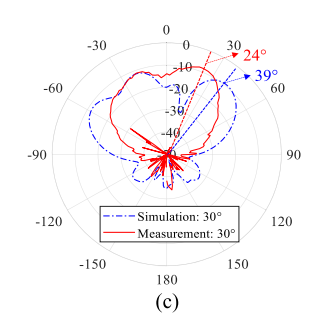


Fig. 12. Comparison of the simulated and measured H-plane radiation pattern ($|S_{21}|$ in dB) under the light configuration of peak directions as $\pm 30^{\circ}$ and 0° . (a) Target peak beam direction = 0° . (b) Target peak beam direction = 30° .

 $\label{table II} \mbox{Measured Dynamic Range of } |S_{21}| \mbox{ In the Desired Directions}$

Desired H-plane beam direction	Nearest peak/null direction		Normalized S ₂₁ _{max} (dB)		Normalized $ S_{21} _{min}$ (dB)	Dynamic range
	Peak	Null	Peak	Side lobe	Null	(dB)
-30°	-24°	-30°	-8.3	-11.2	-35.3	27
-20°	-20°	-18°	-6.2	-11.5	-27.8	21.6
-10°	-10°	-8°	-5.8	-12	-23.3	17.5
0°	3°	0°	-7.5	-21.8	-20.6	13.1
10°	10°	12°	-6	-60	-21.7	15.7
20°	20°	20°	-6.2	-12	-27.2	21
30°	24°	36°	-8.1	-10.4	-44.2	36.1

fine-tuned to optimize the desired maximum or minimum response. The corresponding light configurations after the search algorithm are shown in Table I. The optimized H-plane radiation patterns (normalized $|S_{21}|$) with the desired peak and null directions are shown in Fig. 10. The total radiation pattern is the superposition of the radiated EM wave from each unit cell. Therefore, in some directions, peaks in the radiation pattern can be observed because the phase relationship of the transmitted EM waves between the unit cells added up in those directions. Similarly, nulls in the radiation pattern occur because the phase relationship of the transmitted EM waves between the unit cells is canceled. However, the searching algorithm is just a procedure of trial and error, recording the measured directions of the maximal/minimal radiation under certain random light configuration and comparing that with the target angle of peak/null. For example, under the target of finding a light configuration of generating a null at the normal direction (0°), the algorithm outputs a light configuration shown in the third row and fifth column of Table I, and the corresponding radiation pattern is shown as the purple curve in Fig. 10(b).

Similarly, the corresponding E-plane radiation patterns measured under the same light configurations as in Fig. 10 are shown in Fig. 11. It is observed that no corresponding beam steering happens to the E-plane radiation pattern since the current searching algorithm only takes the local minimum or maximum in the measured H-plane radiation patterns as a goal for identifying the light configurations of certain beamforming. Therefore, the beams in the E-plane radiation patterns are not necessarily to be steered accordingly.

Within a maximal error of 6° , the searching algorithm was able to identify local maxima or minima around the desired peak/null in the radiation pattern among all the light configurations. As a result, the transmit array was able to redirect the local peak of the beam within $\pm 24^{\circ}$ and the local null of the beam within -30° to 36° . The dynamic range of $|S_{21}|$ under different directions is shown in Table II. Besides, when targeting a certain peak beam direction, the sidelobe is calculated and listed in Table II. In scenarios of EM scanning,

a sidelobe of around 6 dB reduction from the main beam could be enough. The algorithm can be improved by limiting the reduction of the sidelobe from the main beam as an extra condition.

B. Comparison Between Simulation and Measurement

Taking the target peak beam directions of $\pm 30^{\circ}$ and 0° as examples, Fig. 12 compares the normalized radiation patterns from measurement and simulation for the same light configurations listed in Table II. The simulated and measured radiation patterns and the corresponding main beam directions are marked as blue and red. Although discrepancies are observed in the shapes of the measured and simulated radiation patterns, which are mainly the different sidelobes, the direction of the simulated and measured main beams under the same light configuration shows a similar trend following the target directions. Quantitatively, the differences in the main beam directions between the measurement and simulation are 1°, 3°, and 15° for the target main beam direction of 0° , -30° , and 30° , respectively. These discrepancies are mainly due to the differences between the simulation model and the actual measurement system, and variations in the light intensity versus dc voltage for individual solar cells. Overall, the similar trend of the main beam directions obtained from the measurement and simulation under the same light configuration proves the validity of the beam searching algorithm and the concept of the optical-controlled design with solar cells for beamforming.

C. Discussion

From the measurement results, if all the unit cells receive the same light intensity, a phase shift of 92° can be achieved at 4.26 GHz for different light intensities. For different light distribution patterns, the beam could be shifted by 30°. However, due to the simplicity of the 4×4 transmit array and the manufacturing variations of the unit cells, performances, such as narrow beam steering and high gain, could not be achieved, as shown in Figs. 5 and 10. The limitations of the 4 × 4 transmit array design in this communication are due to three reasons: 1) the size of the transmit array (4×4) is not large enough; 2) for the current design, the phase shift of the structure can only achieve 92° for the same light intensity illuminating all the unit cells; and 3) the beamwidth for the transmitted wave is wide and the gain for the transmitted wave is low. Methods to improve the beamwidth and tunable range of beam direction are: 1) increasing the array size; 2) adding more phase shifters; and 3) embedding more directional antennas to the top and bottom layers of the transmit array. If applied these methods in the future, a higher gain of the transmit array can be achieved.

The reconfiguration time for beam tuning of the light-controlled transmit array depends on the refresh rate of the projector, which is normally 60 Hz (16.7 ms). Although the reconfiguration time is

slower than the scenario discussed in [33], it can still be applied to scenarios without requiring extremely fast reconfiguration time, such as emission source microscopy [34]. In addition, compared to the traditional reconfigurable antennas with electrical control for phase shifting, this light-modulated method can significantly avoid redundant electrical connections for phase shift controlling, which can reduce the risk of issues related to electrical control and connection. Besides, the light-controlled transmit array uses true wireless power, i.e., no wired power is needed to attach to the transmit array for phase control. Therefore, it is easy to be installed and highly preferred to be used in scenarios where it is challenging to attach power to the traditional electric-controlled transmit array.

IV. CONCLUSION

This communication presents a proof-of-concept for a slide-projector-controlled transmit array and validates the concept by measuring the radiation patterns under different light configurations. By adding a solar cell in each unit cell design, the bias signal of the varactor diodes can be controlled by the external light from a slide projector instead of following the traditional way of using electrical signals generated by a microcontroller. A searching algorithm is created to find the light configurations that can achieve local peaks or nulls in the radiation pattern to meet the desired directions. The designed 4 \times 4 transmit array can achieve a beamforming range of $\pm 24^{\circ}$ in terms of peaks and -30° to 36° in terms of nulls. This concept can be extended to larger arrays. The larger the array, the more advantages can be provided by the control from economical slide projectors or similar devices to achieve a fast millisecond response over a wide area range.

REFERENCES

- L.-Z. Song, P.-Y. Qin, and Y. J. Guo, "A high-efficiency conformal transmitarray antenna employing dual-layer ultrathin Huygens element," *IEEE Trans. Antennas Propag.*, vol. 69, no. 2, pp. 848–858, Aug. 2020.
- [2] J. Yin, Y. Zhang, G. Deng, R. Chen, and H. Chen, "Ultra-wideband transmitarray antennas design based on ultrathin polarization conversion elements," in *Proc. IEEE Asia–Pacific Microw. Conf. (APMC)*, Singapore, Dec. 2019, pp. 423–425.
- [3] F. Wu, J. Wang, R. Lu, X. Xia, W. Hong, and K.-M. Luk, "Wideband and low cross-polarization transmit array using 1-bit magneto-electric dipole elements," *IEEE Trans. Antennas Propag.*, vol. 69, no. 5, pp. 2605–2641, Oct. 2020.
- [4] J. Y. Lau and S. V. Hum, "Reconfigurable transmit array design approaches for beamforming applications," *IEEE Trans. Antennas Propag.*, vol. 60, no. 12, pp. 5679–5689, Dec. 2012.
- [5] K. Pham et al., "Design of wideband dual linearly polarized transmitarray antennas," *IEEE Trans. Antennas Propag.*, vol. 64, no. 5, pp. 2022–2026, May 2016.
- [6] G. Mansutti et al., "Modeling and design of a plasma-based transmitarray with beam scanning capabilities," *Results Phys.*, vol. 16, Mar. 2020, Art. no. 102923.
- [7] G. Mansutti et al., "Design of a hybrid metal-plasma transmit-array with beam-scanning capabilities," *IEEE Trans. Plasma Sci.*, vol. 50, no. 3, pp. 662–669, Mar. 2022.
- [8] L. D. Palma, A. Clemente, L. Dussopt, R. Sauleau, P. Potier, and P. Pouliguen, "1-bit reconfigurable unit cell for Ka-band transmit arrays," *IEEE Antennas Wireless Propag. Lett.*, vol. 15, pp. 560–563, 2016.
- [9] F. Diaby, A. Clemente, L.D. Palma, L.K. Pham, E. Fourn, and R. Sauleau, "Design of a 2-bit unit-cell for electronically reconfigurable transmit arrays at Ka-band," in *Proc. Eur. Radar Conf. (EURAD)*, Nuremberg, Germany, 2017, pp. 473–476.
- [10] A. Clemente, L.D. Palma, F. Diaby, L. Dussopt, K. Pham, and R. Sauleau, "Electronically-steerable transmit array antennas for Ka-band," in *Proc. 13th Eur. Conf. Antennas Propag.*, Krakow, Poland, 2019, pp. 1–4.
- [11] A. Clemente, L. Dussopt, R. Sauleau, P. Potier, and P. Pouliguen, "Wideband 400-element electronically reconfigurable transmit array in X band," *IEEE Trans. Antennas Propag.*, vol. 61, no. 10, pp. 5017–5027, Oct. 2013.

- [12] C.-C. Cheng, B. Lakshminarayanan, and A. Abbaspour-Tamijani, "A programmable lens-array antenna with monolithically integrated MEMS switches," *IEEE Trans. Microw. Theory Techn.*, vol. 57, no. 8, pp. 1874–1884, Aug. 2009.
- [13] L. Dussopt et al., "A V-band switched-beam linearly polarized transmitarray antenna for wireless backhaul applications," *IEEE Trans. Antennas Propag.*, vol. 65, no. 12, pp. 6788–6793, Dec. 2017.
- [14] J. Y. Lau and S. V. Hum, "A wideband reconfigurable transmit array element," *IEEE Trans. Antennas Propag.*, vol. 60, no. 3, pp. 1303–1311, Mar. 2012.
- [15] P. Padilla, A. Muñoz-Acevedo, M. Sierra-Castañer, and M. Sierra-Pérez, "Electronically reconfigurable transmit array at Ku band for microwave applications," *IEEE Trans. Antennas Propag.*, vol. 58, no. 8, pp. 2571–2579, Aug. 2010.
- [16] S. Bildik et al., "Reconfigurable liquid crystal reflectarray with extended tunable phase range," in *Proc. 41st Eur. Microw. Conf.*, Manchester, U.K., 2011, pp. 1292–1295.
- [17] S. Bildik, S. Dieter, C. Fritzsch, W. Menzel, and R. Jakoby, "Reconfigurable folded reflectarray antenna based upon liquid crystal technology," *IEEE Trans. Antennas Propag.*, vol. 63, no. 1, pp. 122–132, Jan. 2015.
- [18] Y. Zhao, C. Huang, A.-Y. Qing, and X. Luo, "A frequency and pattern reconfigurable antenna array based on liquid crystal technology," *IEEE Photon. J.*, vol. 9, no. 3, pp. 1–7, Jun. 2017.
- [19] P. V. Kapitanova, S. I. Maslovski, I.V. Shadrivov, P. A. Belov, and Y. S. Kivshar, "Light-controllable split-ring resonators," in *Proc.* 42nd Eur. Microw. Conf., Amsterdam, The Netherlands, Oct. 2012, pp. 582–584.
- [20] P. Kapitanova et al., "Light-controllable magnetic metamaterials based on loaded split-ring resonators," in *Proc. IEEE Int. Symp. Antennas Propag.*, Chicago, IL, USA, Jul. 2012, pp. 1–2.
- [21] A. P. Slobozhanyuk et al., "Photosensitive SRR-metamaterials," in *Proc. IEEE Antennas Propag. Soc. Int. Symp. (APSURSI)*, Orlando, FL, USA, Jul. 2013, pp. 1190–1191.
- [22] X.G. Zhang, W. X. Tang, W. X. Jiang, G. D. Bai, C.-W. Qiu, and T. J. Cui, "Light—Controllable digital coding metasurfaces," Adv. Sci., vol. 5, May 2018, Art. no. 1801028.
- [23] H. A. E.-A. Malhat, M. M. Badawy, S. H. Zainud-Deen, and K. H. Awadalla, "Dual-mode plasma reflectarray/transmitarray antennas," *IEEE Trans. Plasma Sci.*, vol. 43, no. 10, pp. 3582–3589, Oct. 2015.
- [24] C. Gong, W. Su, Y. Zhang, P. Chen, and W. Liu, "An active metamaterials controlled by structured light illumination," *Optik*, vol. 171, pp. 204–209, Oct. 2018.
- [25] H. Y. Tang, R. S. Donnan, and T. Kreouzis, "An optically controlled phase shifter employing the organic semiconductor poly (3-hexylthiophene)," Appl. Phys. Lett., vol. 91, Nov. 2007, Art. no. 202101.
- [26] A. Andy, R. Dubrovka, T. Kreouzis, and R. S. Donnan, "An optically controlled phase shifter for antenna array beam steering," in *Proc. 9th Eur. Conf. Antennas Propag. (EuCAP)*, 2015, pp. 1–4.
- [27] A. S. Andy, J. W. E. Kneller, R. Dubrovka, T. Kreouzis, and R. Donnan, "Antenna array control via integrated optically-activated organic semiconductor for S-band applications," in *Proc. 46th Eur. Microw. Conf. (EuMC)*, London, U.K., Oct. 2016, pp. 1291–1294.
- [28] W. M. Manheimer, "Plasma reflectors for electronic beam steering in radar systems," *IEEE Trans. Plasma Sci.*, vol. 19, no. 6, pp. 1228–1234, Dec. 1991.
- [29] S. Chaimool, C. Rakluea, and P. Akkaraekthalin, "Mu-near-zero metasurface for microstrip-fed slot antennas," *Appl. Phys. A, Solids Surf.*, vol. 112, no. 3, pp. 669–675, 2013.
- [30] M. Havrilla, A. Bogle, and M. Hyde, "Improved bandwidth in rectangular waveguide material characterization measurements," in *Proc. Antenna Meas. Tech. Associat. Annu. Symp.*, Tucson, AZ, USA, 2014, pp. 427–431.
- [31] UWB-4 1.8 GHz-9 GHz Wideband Omnidirectional Antenna, DEEP-ACE. [Online]. Available: https://deepace.net/product/uwb-4-1-8ghz-9ghz-wideband-omnidirectional-antenna-copy/
- [32] Eccorsorb QR-13 AF, Laird. Accessed: Aug. 3, 2022. [Online]. Available: https://www.laird.com/sites/default/files/2022-03/RFP-DS-QR%2013%20AF%2003082022.pdf
- [33] Q. Wu, S. Zhang, B. Zheng, C. You, and R. Zhang, "Intelligent reflecting surface-aided wireless communications: A tutorial," *IEEE Trans. Commun.*, vol. 69, no. 5, pp. 3313–3351, May 2021.
- [34] P. Maheshwari, H. Kajbaf, V. V. Khilkevich, and D. Pommerenke, "Emission source microscopy technique for EMI source localization," *IEEE Trans. Electromagn. Compat.*, vol. 58, no. 3, pp. 729–737, Jun. 2016.